First ENA observations at Mars: ENA emissions from the martian upper atmosphere

Y. Futaana [a,*], S. Barabash [a], A. Grigoriev [a], M. Holmström [a,b], E. Kallio [c], P. C:son Brandt [d],
H. Gunell [a], K. Brinkfeldt [a], R. Lundin [a], H. Andersson [a], M. Yamauchi [a], S. McKenna-Lawler [e],
J.D. Winningham [f], R.A. Frahm [f], J.R. Sharber [f], J.R. Scherrer [f], A.J. Coates [g], D.R. Linder [g],
D.O. Kataria [g], T. Säles [c], P. Riihelä [c], W. Schmidt [c], H. Koskinen [h], J. Kozyra [i], J. Luhmann [j],
E. Roelof [c], D. Williams [c], S. Livi [c], C.C. Curtis [k], K.C. Hsieh [k], B.R. Sandel [k], M. Grande [l],
M. Carter [l], J.-A. Sauvaud [m], A. Fedorov [m], J.-J. Thocaven [m], S. Orsini [n], R. Cerulli-Irelli [n],
M. Maggi [n], P. Wurz [o], P. Bochsler [o], A. Galli [o], N. Krupp [p], J. Woch [p], M. Fränz [p],
K. Asamura [q], C. Dierker [r]

[a] Swedish Institute of Space Physics, Box 812, SE-981 28 Kiruna, Sweden
[b] NASA Goddard Space Flight Center, Greenbelt, MD 20771, USA
[c] Finnish Meteorological Institute, Box 503, FIN-00101 Helsinki, Finland
[d] Applied Physics Laboratory, Johns Hopkins University, Laurel, MD 20723-6099, USA
[e] Space Technology Ireland, National University of Ireland, Maynooth, Co. Kildare, Ireland
[f] Southwest Research Institute, San Antonio, TX 7228-0510, USA
[g] Mullard Space Science Laboratory, University College London, Surrey RH5 6NT, UK
[h] University of Helsinki, Department of Physical Sciences, P.O. Box 64, 00014 Helsinki, Finland
[i] Space Physics Research Laboratory, University of Michigan, Ann Arbor, MI 48109-2143, USA
[j] Space Science Laboratory, University of California in Berkeley, Berkeley, CA 94720-7450, USA
[k] University of Arizona, Tucson, AZ 85721, USA
[l] Rutherford Appleton Laboratory, Chilton, Didcot, Oxfordshire OX11 0QX, UK
[m] Centre d'Etude Spatiale des Rayonnements, BP-4346, F-31028 Toulouse, France
[n] Istituto di Fisica dello Spazio Interplanetari, I-00133 Rome, Italy
[o] Physikalisches Institut, University of Bern, CH-3012 Bern, Switzerland
[p] Max-Planck-Institut für Aeronomie, D-37191 Katlenburg-Lindau, Germany
[q] Institute of Space and Astronautical Science, 3-1-1 Yoshinodai, Sagamihara, Japan
[r] Technical University of Braunschweig, Hans-Sommer-Strasse 66, D-38106 Braunschweig, Germany

Abstract

The neutral particle detector (NPD) on board Mars Express has observed energetic neutral atoms (ENAs) from a broad region on the dayside of the martian upper atmosphere. We show one such example for which the observation was conducted at an altitude of 570 km, just above the induced magnetosphere boundary (IMB). The time of flight spectra of these ENAs show that they had energies of 0.2–2 keV/amu, with an average energy of $\sim$1.1 keV/amu. Both the spatial distribution and the energy of these ENAs are consistent with the backscattered ENAs, produced by an ENA albedo process. This is the first observation of backscattered ENAs from the martian upper atmosphere. The origin of these ENAs is considered to be the solar wind ENAs that are scattered back by collision processes in the martian upper atmosphere. The particle flux and energy flux of the backscattered ENAs are 0.9–1.3 $\times 10^7$ cm^{-2} s^{-1} and $\sim$9.5 $\times 10^9$ eV cm^{-2} s^{-1}, respectively.
© 2005 Elsevier Inc. All rights reserved.

* Corresponding author. Fax: +46 980 79091.
  E-mail address: futaana@irf.se (Y. Futaana).

1. Introduction

Energetic neutral atom (ENA) imaging in space provides a means to investigate the interaction between space plasmas and neutral atoms. The first dedicated ENA instrument was carried by the Swedish satellite Astrid-1 (Barabash, 1995). The dynamics of the terrestrial ionosphere and magnetosphere are visualized by ENAs (e.g., Barabash et al., 1998; C:son Brandt et al., 2001). Since then many spacecraft have carried ENA imagers on terrestrial and planetary missions. Cassini was the first spacecraft that carried an ENA instrument (MIMI/INCA) to Saturn.

Mars Express brought two ENA instruments to Mars for the first time: the neutral particle imager (NPI) and the neutral particle detector (NPD), as parts of a plasma and neutral particle package called the Analyser of Space Plasma and EneRgetic Atoms (ASPERA-3). The NPI is designed to measure ENAs with good angular resolution, and the NPD is designed to resolve energy and mass of ENAs but with relatively coarse angular resolution and more limited angular coverage (Barabash et al., 2004).

Since Mars has no global intrinsic magnetic field like the Earth (e.g., Acuña et al., 1998), the solar wind can directly interact with the martian exosphere. Therefore ENA sources around Mars are expected to be quite different from those around the Earth (Barabash et al., 2004, and references therein). Barabash et al. (2004) enumerated possible ENA sources: the supersonic solar wind (Holmström et al., 2002), the shocked solar wind (Holmström et al., 2002), accelerated planetary ions (Barabash et al., 2002; Lichtenegger et al., 2002), solar wind protons interacting with the tenuous Phobos atmosphere (Mura et al., 2002), atmospheric atoms sputtered by picked-up O^+ ions (Luhmann and Bauer, 1992), and solar wind ENAs backscattered from the martian exosphere (an ENA albedo process) (Kallio and Barabash, 2001; Holmström et al., 2002).

In the present study, we focus on ENA observations when the NPD was looking down at the martian subsolar region and conditions for the observation of backscattered ENAs were favorable.

The generation mechanism of backscattered ENAs is as follows. When solar wind protons approach Mars, some of the protons are neutralized through charge exchange with planetary exospheric particles. The generated hydrogen ENAs (solar wind ENAs) have the same energy as the solar wind protons. They can penetrate below the plasma boundary called the induced magnetosphere boundary (IMB, see Lundin et al., 2004). When these solar wind ENAs reach the exobase, they experience elastic and inelastic collisions (Kallio and Barabash, 2000), and some of them are scattered back. Kallio and Barabash (2001) used a three-dimensional Monte Carlo model to investigate these backscattered ENAs. The ratio of the particle flux of the backscattered ENAs to the impinging ENAs was found to be 0.58. The average energy of the backscattered ENAs was ~60% that of the impinging ENAs.

In addition to the solar wind ENAs, solar wind protons may also reach the exobase because of their finite gyroradius (Brecht, 1997), even if the bulk flow cannot enter below the IMB. Those protons reaching the exobase experience the similar elastic and inelastic collision processes and a proportion of them are scattered back as hydrogen atoms. We call this mechanism 'proton-ENA albedo process' hereafter. The ENA flux generated by this proton-ENA albedo process was mentioned by Holmström et al. (2002). They used the proton precipitation flux calculated by Brecht (1997), and concluded that the flux of ENAs associatively produced is small enough to be neglected.

The NPD observed the backscattered ENAs from the martian upper atmosphere during its initial-phase observations when the observational conditions and instrument operation mode were particular favorable. This is the first observation of backscattered ENAs from the upper atmosphere of an unmagnetized planet. We will present below a typical example of backscattered ENAs recorded by the NPD and discuss their general characteristics.

2. Instrumentation

The Analyser of Space Plasma and EneRgetic Atoms (ASPERA-3) instrument on board Mars Express consists of four sensors, an ion mass analyser (IMA), an electron spectrometer (ELS), a neutral particle imager (NPI), and a neutral particle detector (NPD) (Barabash et al., 2004).

The NPD is made up of two identical detectors called NPD-1 and NPD-2. The only difference between them is the respective directions of their fields of view (cf. Fig. 1 of Futaana et al. (2006), in this issue). The NPD measures the ENA differential flux over the energy range 100 eV to 10 keV, while resolving H and O. Each detector has a $9 \times 90°$ intrinsic field of view and the aperture is divided into three directions (Dirs 0, 1, and 2). Each direction is covered by an independent sensor with an angular resolution of ~$5 \times 40°$ (full width at half maximum). This means that a slight overlap of viewing angles exist to provide complete angular coverage.

The principle of ENA measurements by the NPD is summarized as follows. An incident ENA that impact a START surface produces secondary electrons, that are transported to an MCP (microchannel plate) assembly to give a START signal. An electrostatic deflector is placed in front of the aperture to remove charged particles. The incident ENA that impacts the START surface is reflected there, and then travels to a STOP surface, where secondary electrons are newly generated to provide a STOP signal. There are three STOP surfaces, 30° apart each other, that correspond to different directions of the incident ENAs. By taking the one-to-one coincidence between START and STOP signals within a certain window, the time-of-flight (TOF) of the particle is obtained. The TOF is converted to particle velocity by using the distance between the START and STOP surfaces (8.0 cm). Particles lose ~33% of their energy during their interaction with the START surface and the

velocity should be corrected correspondingly. The TOF analysis can eliminate false counts due to ultraviolet (UV) radiation (Brinkfeldt et al., 2006) because UV counts have very short TOFs. The Pulse-height (PH) distribution of the STOP signals can provide a rough estimation of the species between proton and oxygen. The geometrical factor (G_0) and the efficiency (ε) are obtained from ground calibration data. The product of these quantities is $\varepsilon \cdot G_0 \sim 9.78 \times 10^{-5}$ cm^2 sr in case of 0.7 keV hydrogen atoms.

The NPD has several observation modes. The mode in operation during the observations reported in the present paper is the so-called 'raw' mode. Due to limited memory size, only the first 512 STOP signals during every second are recorded with information concerning direction, TOF (11 bits), PH (8 bits) and the coincidence with START signals. In these 512 records, there exist invalid data, i.e. one-to-one coincidences between the START and STOP signals cannot be found. After downlink of the data, we select only the valid records (i.e. the records having one-to-one coincidence between START and STOP signals). For those, we obtain the velocity, the pulse height and the count rate of the impinging ENAs. Since the count rates at the STOP surface are normally larger than 512 counts/s, the memory is filled in less than 1 s. This means that the accumulation time, Δt, is shorter than 1 s. Δt is calculated as follows

$$\Delta t = 512/C_{\text{stop}}, \tag{1}$$

where C_{stop} is the count rate (counts/s) at the STOP surfaces. Using the accumulation time of Δt, we can infer the valid count rate of ENAs, C_{ENA}, as

$$C_{\text{ENA}} = N_{\text{valid}}/\Delta t, \tag{2}$$

where N_{valid} is the number of valid data contained in the 512 records.

3. Observation

In this section, we present an example of an NPD observation of the backscattered ENAs. The observation was made on 27 Feb. 2004, when the pericenter of Mars Express was very close to the subsolar point. The observation mode of the NPD was raw mode, in which detailed TOF spectra can be obtained. Due to the Mars Express position and the operation mode of the NPD, the best possible opportunity was provided to detect ENAs from the martian upper atmosphere and to institute a detailed analyses of these data.

The orbit of Mars Express on 27 Feb. 2004 is shown in Fig. 1. Here we have adopted the cylindrical Mars–Sun orbit (MSO) coordinate system. The MSO system is defined in such a way that the x-axis points from the center of Mars to the Sun, the z-axis is perpendicular to the martian orbital plane and the y-axis completes the right-hand system. The vertical axis in Fig. 1 is the distance from the Mars–Sun line ($r = \sqrt{y^2 + z^2}$). The pericenter was at 19:40 UT with a height of $\sim$270 km.

The dashed lines show the modeled locations of the Bow Shock (BS) and the Magnetic Pileup Boundary (MPB) calculated from the empirical model derived from Mars Global Surveyor (MGS) observations (Vignes et al., 2000). According
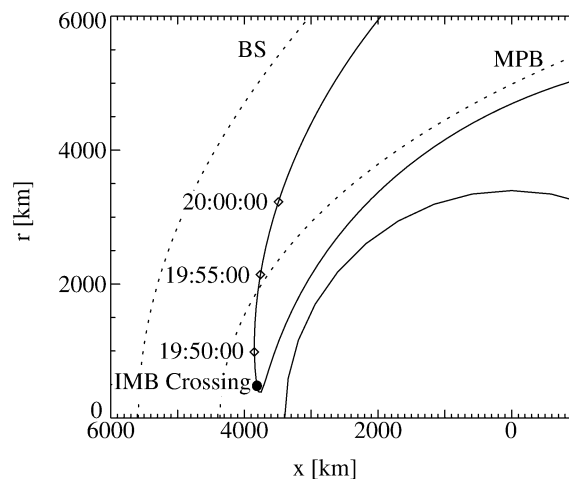

Fig. 1. Orbit of the Mars Express on 27 Feb. 2004. The MSO-cylindrical coordinate system is used. Dashed lines correspond to the bow shock (BS) and the magnetic pileup boundary (MPB) modeled by Vignes et al. (2000). The location of the IMB crossing is shown by the solid circle.

to this figure, the spacecraft should cross the MPB at $\sim$19:54 UT. However, the in situ observation of the ion mass analyser and electron sensor on board Mars Express encountered the boundary at $\sim$19:47–48 UT at a height of 420–460 km (the filled circle in Fig. 1), thereby indicating that the induced magnetosphere boundary was located at a lower altitude than the modeled MPB during the observation interval. (IMB is defined as the envelope of induced martian magnetosphere, i.e. the stopping boundary for the solar wind protons (Lundin et al., 2004).) Although the relation between the MPB (defined by magnetometer) and the IMB (defined by plasma instruments) is not presently known, they are believed to be closely located. Therefore it is possible that solar wind dynamic pressure was higher than its average value. Unfortunately, the solar wind conditions are not available because the IMA and ELS ceased operations at $\sim$20:00 UT while Mars Express was still in the magnetosheath.

Fig. 2 displays the NPD-2 observation made between 19:50 and 19:55 UT on 27 Feb. 2004, when Mars Express was above the IMB (570–930 km). The left panels show the TOF spectrograms corresponding to the three directions. The right panels display TOF spectra integrated over the 5 min observation time for each direction. Dashed lines indicate the background count levels in each direction as defined by the low energy channel (corresponding to 7.96–14.2 eV/amu or TOF $\sim$ 1534–2048 ns). The TOF distribution has a broad spectrum at a range of 150–500 ns (0.2–2.3 keV/amu), with a sharp peak embedded at 150–300 ns (0.6–2.3 keV/amu). Another observation was made under similar conditions and in the same observation mode between 17:20–17:24 UT on 29 Feb. 2004. The results are very similar to those shown in Fig. 2.

The time series of the count rates of ENAs integrated over the TOF range of 0–2048 ns is shown in Fig. 3. The accumulation time of each sample (1 s) is calculated to be $\sim$36 ms from Eq. (1). The calculated background level was subtracted before the integration. We can thus derive the differential flux of ENAs. The count rate for each direction was constantly 150–200 counts/s throughout the observation. Using the geometrical
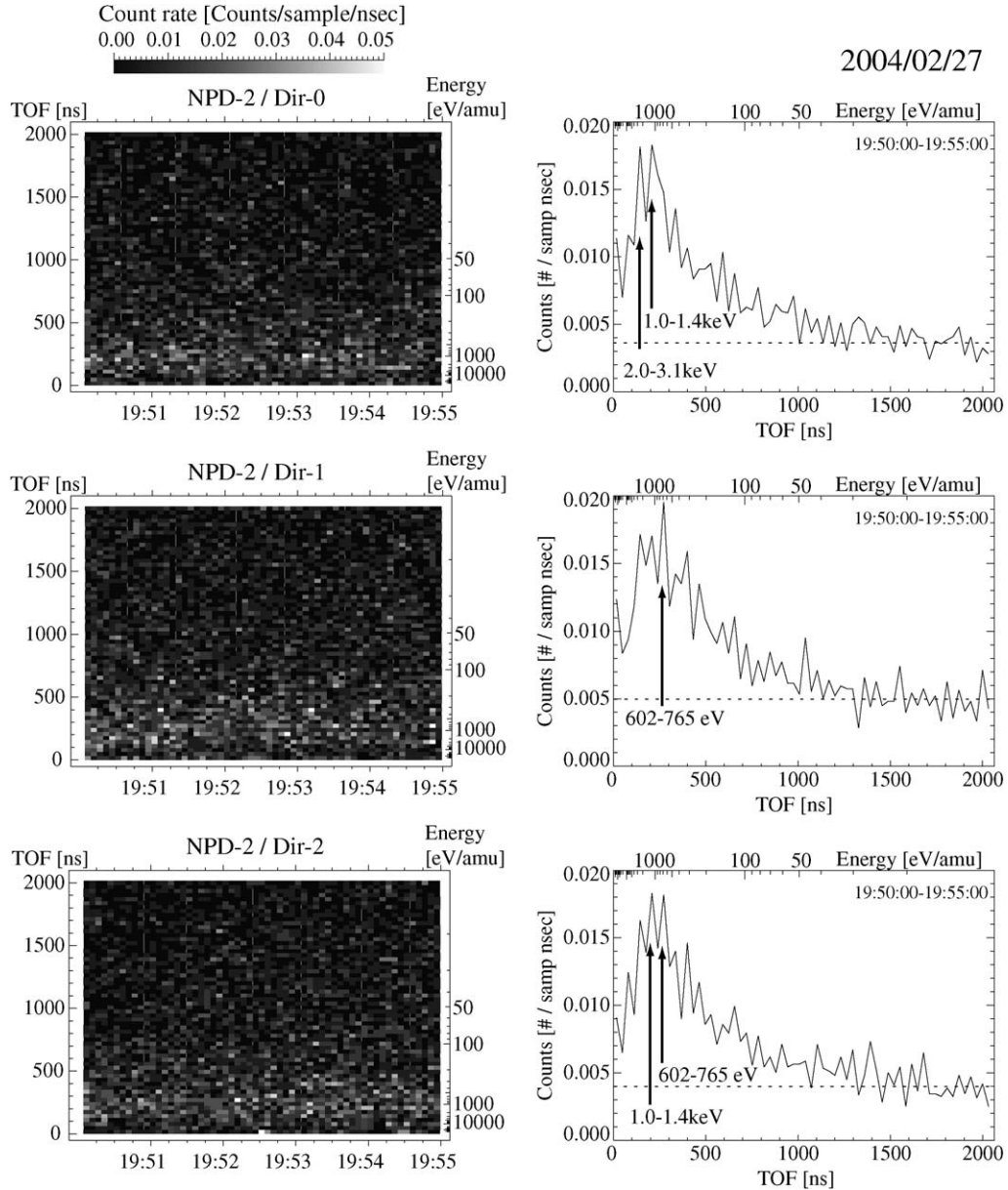
Fig. 2. NPD observations conducted between 19:50 and 19:55 UT on 27 Feb. 2004. From top to bottom, three directions of NPD-2 are shown. The left panels show the TOF spectrograms and the right panels show the corresponding TOF spectra integrated over the 5-min observation. The dashed lines in the right panels indicate the noise level of each channel. In all panels, the data are integrated over every 32 ns in TOF bins and every 5 s in UT bins.

factor and the efficiency ($\varepsilon \cdot G_0 \sim 1 \times 10^{-4}$ for 700 eV protons), we obtain a differential flux of $J \sim 1.5$–2.0×10^6 cm^{-2} sr^{-1} s^{-1}. Assuming that the emission of the observed ENAs is isotropic, the particle flux of the generated ENAs is also calculated as $F = 0.94$–1.26×10^7 cm^{-2} s^{-1}.

Fig. 4 shows the 3D geometry of the NPD field of view (FOV) at 19:50 UT and at 19:55 UT on 27 Feb. 2004 in the MSO coordinate system. The white line represents the Mars Express trajectory and the solid angles correspond to the NPD-2 FOVs. The solid lines at the martian surface correspond to the Sun–Mars meridian and the equator in the MSO coordinate system, and the subsolar point is indicated by the filled circle. The dashed lines correspond to longitude and latitude

every 30°. The FOV pointed toward the planet throughout the observation. The coverage of the FOV is from the subsolar point to 30° N.

4. Discussion

The NPD has detected ENAs at an altitude of 570 km (19:50 UT) while the IMB was at 420–460 km near the subsolar point. Since the NPD was looking at the planet all the time as shown in Fig. 4, the ENAs are most likely to come from the martian upper atmosphere because the bulk velocity of the shocked solar wind was nearly perpendicular to the NPD view direction.

The count rates of the observed ENAs shown in Fig. 3 did not change significantly with time, even though the count rate
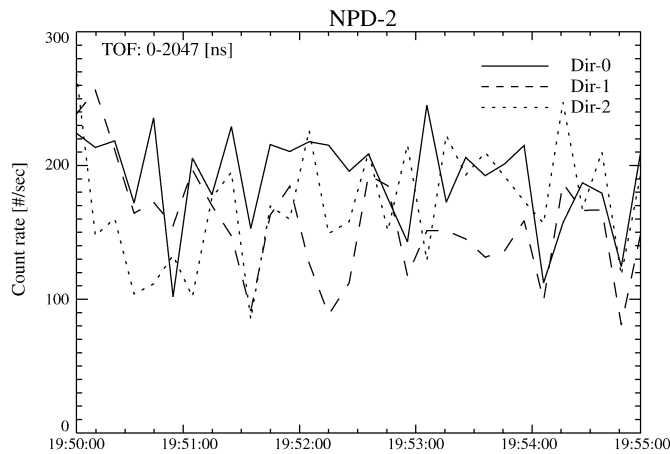
Fig. 3. Time series of the count rates of ENAs integrated over the TOF range 0–2048 ns. Background counts have been subtracted. The solid, dashed, and dotted lines correspond to Dir 0, 1, and 2, respectively. The data are averaged over every 10 s.
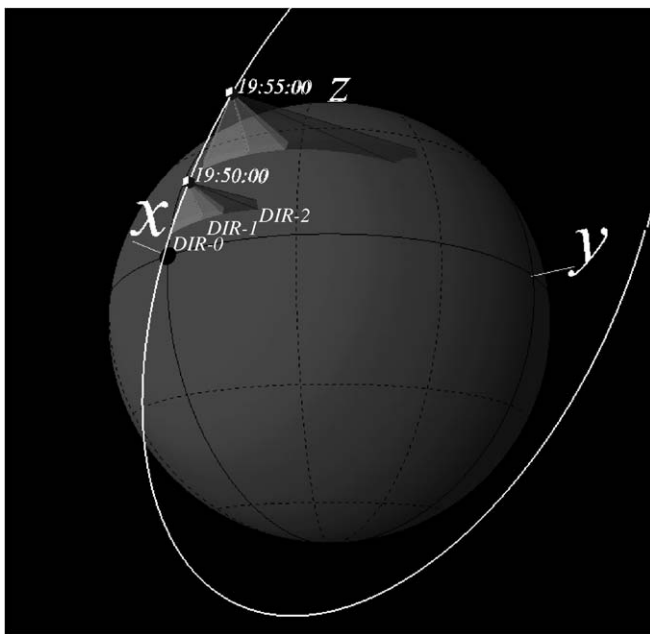

Fig. 4. The 3D geometry of the FOV of the NPD-2 during the observations (19:50–55 UT). The MSO coordinate system is used; the x-axis is the Mars–Sun line. The white line is the orbit of Mars Express and the transparent solid angles are the FOVs of the three directions of NPD-2. The dashed lines are the longitude and latitude lines at every 30° and the black filled circle indicates the subsolar point.

showed a large fluctuation. The fluctuation is most likely due to the short integration time on board of each sample (~3.6% of total time). The fact that the count rate was constant with time indicates that the ENAs were emitted from a broad region of the martian upper atmosphere; at least from the area with solar zenith angle of <30° that the FOV of the NPD-2 covered (Fig. 4). The characteristics of a wide generation region agrees with the predicted ENA albedo.

The energy of the detected ENAs was 0.2–2.3 keV/amu. If the ENAs were oxygen atoms, their energy would be 3.2–36.8 keV. This is not realistic because no acceleration mechanisms of oxygen up to 30 keV below the altitude of 570 km are

expected. Also, the ion mass analyser (IMA) on board Mars Express has not detected such high energy oxygen (Lundin et al., 2004). Therefore, the observed ENAs are most likely to be the hydrogen atoms.

The observed energy of 0.2–2.3 keV corresponds to 200–660 km/s. The average energy of the ENAs is ~1.1 keV derived from the TOF spectra in the TOF range of 70–710 ns, corresponding to an energy range between 100 eV and 10 keV. The particle flux is estimated as $F = 0.94$–1.26×10^7 cm^{-2} s^{-1}.

Kallio and Barabash (2001) made a 3D Monte Carlo model of precipitating ENAs and discussed characteristics of backscattered ENAs. The velocity distribution of backscattered ENAs is very broad (50–450 km/s) in their ENA albedo model. This is in good agreement with the observed broadness and velocity. However, the particle flux is slightly different. Kallio and Barabash (2001) used typical solar wind parameters of the velocity ($v = 400$ km/s) and the density ($n = 2.5$/cc), and derived the precipitating ENA flux at the subsolar point to be 5.5×10^6 cm^{-2} s^{-1}, and that 58% of them are scattered back as ENA albedo. This means that an ENA flux of 3.2×10^6 cm^{-2} s^{-1} is theoretically expected at around the subsolar point, which is consistent with but smaller than the observed ENA flux by a factor of 3–4.

To investigate why the observed ENA flux was 3–4 times higher than its theoretical value, we have to know the solar wind flux. Since Mars Express was inside the bow shock, we do not know the undisturbed solar wind parameters. However, we can make a rough estimation of the solar wind flux based on the magnetosheath observations. From the IMA data, we can derive the shocked solar wind velocity as $\vec{V}_{sh} \sim (-4.4 \times 10^2$ km/s, 4.0×10^2, 1.6×10^1) in the MSO coordinate system. The density is estimated as $n_{sh} = 3$–4/cm^3 from the ELS data. Assuming conservation of the solar wind flux in the x-direction (i.e. assuming a one-dimensional variation along the solar wind flow direction), the solar wind flux can be estimated as $n_{sh} \cdot V_{x,sh} = 1.3$–$1.8 \times 10^8$ cm^{-2} s^{-1}.

This value is higher than the flux used in the model by Kallio and Barabash (2001), which is 1×10^8 cm^{-2} s^{-1}. This difference might explain the high flux of the observed ENAs. However, we have to mention that the derived solar wind flux can be overestimated. Considering MHD shock theories, the velocity in the magnetosheath >400 km/s implies the velocity ~1000 km/s in the undisturbed upstream region. This is extremely high. Since the subsolar magnetosheath is so compact, kinetic effects can control ion characteristics of the bow shock and the magnetosheath, and then the in situ ion measurement in magnetosheath can show higher velocity than bulk velocity. In this regard, the solar wind flux might be smaller than the estimated value.

There are alternative possibilities to explain the high ENA flux. One is the low altitude of the IMB. The IMB during the observation period was lower than the average. In such a configuration, more solar wind ENAs would be generated, resulting in large backscattered fluxes.

Another candidate is the proton-ENA albedo mechanism. Shocked solar wind ions can penetrate below the IMB due to the finite-gyro radius. Some of these solar wind protons can

interact with the dense atmosphere and experience the same collision processes as penetrating solar wind ENAs. Such protons are scattered back as neutrals. Recent observations revealed that the solar wind protons can penetrate up to 270 km (Lundin et al., 2004) and this means that this proton-ENA albedo mechanism can be more important than expected. This mechanism is mentioned by Holmström et al. (2002). They used a proton precipitation flux of 10^4–10^5 cm^{-2} s^{-1} (Brecht, 1997) and concluded that the proton-ENA albedo mechanism can be negligible. On the other hand, Kallio and Janhunen (2001) concluded that up to 10^8 cm^{-2} s^{-1} protons can precipitate into the martian atmosphere. Assuming the proton-ENA albedo to be 0.58, the backscattered ENA flux due to the proton-ENA albedo mechanism is estimated to be 5.8×10^7 cm^{-2} s^{-1}, which is larger than the observed flux. In this sense, the proton-ENA albedo mechanism can also provide an explanation of the observed high flux. Due to the large difference (3–4 orders) of the precipitating proton flux between the two models, we cannot conclude whether the proton-ENA albedo contributes to the high backscattered ENA flux. We need more precise models of the interaction between the solar wind and Mars to evaluate the effect of proton-ENA albedo quantitatively.

5. Summary

Using NPD data from Mars Express, we have presented an example of the backscattered ENAs from the martian upper atmosphere (ENA albedo process). The NPD has detected the backscattered ENAs at an altitude of 570 km near the subsolar point. This is the first observation of backscattered ENAs from an unmagnetized planetary upper atmosphere.

Let us now summarize several important parameters from the NPD observations. The backscattered ENAs have energies of 0.2–2 keV with an average energy of ~1.1 keV. The distribution and the energy agree well with the results of a Monte-Carlo simulation by Kallio and Barabash (2001). The ratio of the fluxes between the solar wind particles and the backscattered ENAs from the martian upper atmosphere is 5–10% if we employ the roughly estimated solar wind flux of 1.3–1.8×10^8 cm^{-2} s^{-1} and the observed ENA flux of $F = 0.94$–1.26×10^7 cm^{-2} s^{-1}. The energy flux of backscattered ENAs is calculated to be ~9.5×10^9 eV cm^{-2} s^{-1} using the energy range of 100 eV–10 keV. Kallio and Barabash (2001) predicted that 33% of the impinging energy flux of the solar wind ENAs is transported back while 67% is lost around the martian exobase. Using this predicted ratio, the total energy flux deposited in the martian atmosphere is estimated to be ~2×10^{10} eV cm^{-2} s^{-1}.

The observed backscattered ENAs are almost consistent with, but higher than the flux estimated by the theory of ENA albedo (Kallio and Barabash, 2001). There are two other possible explanations: the low altitude IMB and the proton-ENA albedo. To evaluate these effects, we need more precise models of the interaction between the solar wind and Mars.

The next step in the analyses will be to produce ENA albedo maps of the martian upper atmosphere. Comparison between the observed ENA albedo maps and those produced theoreti-

cally (e.g., Holmström et al., 2002) will allow us to infer the interaction between the solar wind and the martian atmosphere, and to estimate the proton precipitation rates in a function of upstream parameters. The ENA albedo is expected to depend on the solar zenith angle (Kallio and Barabash, 2001; Kallio and Janhunen, 2001) and on the upstream conditions. ENA albedo maps can, in principle, be converted to a precipitation map of the solar wind particles (both of ENAs and protons) into the martian upper atmosphere since the backscattered ENAs are directly connected to the precipitation of the solar wind particles into the martian upper atmosphere. These results will also provide information concerning energy and momentum transport from the solar wind into the martian upper atmosphere.

References

Acuña, M.H., Connerney, J.E.P., Wasilewski, P., Lin, R.P., Anderson, K.A., Carlson, C.W., McFadden, J., Curtis, D.W., Mitchell, D., Reme, H., Mazelle, C., Sauvaud, J.A., d'Uston, C., Cros, A., Medale, J.L., Bauer, S.J., Cloutier, P., Mayhew, M., Winterhalter, D., Ness, N.F., 1998. Magnetic field and plasma observations at Mars: Initial results of the Mars Global Surveyor mission. Science 279, 1676–1680.

Barabash, S., 1995. Satellite observations of the plasma-neutral coupling near Mars and the Earth. Ph.D. thesis. Swedish Institute of Space Physics.

Barabash, S., Norberg, O., Lundin, R., Olsen, S., Lundin, K., Brandt, P.C., Roelof, E.C., Chase, C.J., Mauk, B.H., Koskinen, H., Rynö, J., 1998. Energetic neutral atom imager on the Swedish microsatellite Astrid. In: Pfaff, R.F., Borovsky, J.E., Young, D.T. (Eds.), Measurement Techniques in Space Plasmas, Field. In: AGU Geophysical Monographs, vol. 103. American Geophysical Union, Washington, DC, pp. 257–262.

Barabash, S., Holmström, M., Lukyanov, A., Kallio, E., 2002. Energetic neutral atoms at Mars. 4. Imaging of planetary oxygen. J. Geophys. Res. 107 (A10), doi:10.1029/2001JA000326. 1280.

Barabash, S., Lundin, R., Andersson, H., Gimholt, J., Holmström, M., Norberg, O., Yamauchi, M., Asamura, K., Coates, A.J., Linder, D.R., Kataria, D.O., Curtis, C.C., Hsieh, K.C., Sandel, B.R., Fedorov, A., Grigoriev, A., Budnik, E., Grande, M., Carter, M., Reading, D.H., Koskinen, H., Kallio, E., Riihela, P., Säles, T., Kozyra, J., Krupp, N., Livi, S., Woch, J., Luhmann, J., McKenna-Lawlor, S., Orsini, S., Cerulli-Irelli, R., Maggi, M., Morbidini, A., Mura, A., Milillo, A., Roelof, E., Williams, D., Sauvaud, J.-A., Thocaven, J.-J., Moreau, T., Winningham, D., Frahm, R., Scherrer, J., Sharber, J., Wurz, P., Bochsler, P., 2004. ASPERA-3: Analyser of space plasmas and energetic ions for Mars Express. In: Wilson, A. (Ed.), Mars Express: The Scientific Payload. ESA Special Publication SP-1240. ESA Publications Division, Noordwijk, The Netherlands, pp. 121–139.

Brecht, S.H., 1997. Solar wind proton deposition into the martian atmosphere. J. Geophys. Res. 102 (A6), 11287–11294.

Brinkfeldt, K., Gunell, H., Brandt, P., Barabash, S., Frahm, R.A., Winningham, J.D., Kallio, E., Holmström, M., Futaana, Y., Ekenbäck, A., Lundin, R., Andersson, H., Yamauchi, M., Grigoriev, A., Sharber, J.R., Scherrer, J., Coates, A.J., Linder, D.R., Kataria, D.O., Koskinen, H., Säles, T., Riihela, P. , Schmidt, W., Kozyra, J., Luhmann, J., Roelof, E., Williams, D.,

Livi, S., Curtis, C.C., Hsieh, K.C., Sandel, B.R., Grande, M., Carter, M., Sauvaud, J.-A., Fedorov, A., Thocaven, J.-J., McKenna-Lawler, S., Orsini, S., Cerulli-Irelli, R., Maggi, M., Wurz, P., Bochsler, P., Krupp, N., Woch, J., Fraenz, M., Asamura, K., Dierker, C., 2006. First ENA observations at Mars: Solar-wind ENAs on the nightside. Icarus 182, 439–447.

C:son Brandt, P., Barabash, S., Roelof, E.C., Chase, C.J., 2001. Energetic neutral atom imaging at low altitudes from the Swedish microsatellite Astrid: Observations at low ($\leqslant$10 keV) energies. J. Geophys. Res. 106 (A11), 24663–24674.

Futaana, Y., Barabash, S., Grigoriev, A., Holmström, M., Kallio, E., C:son Brandt, P., Gunell, H., Brinkfeldt, K., Lundin, R., Andersson, H., Yamauchi, M., McKenna-Lawler, S., Winningham, J.D., Frahm, R.A., Sharber, J.R., Scherrer, J., Coates, A.J., Linder, D.R., Kataria, D.O., Säles, T., Riihela, P., Schmidt, W., Koskinen, H., Kozyra, J., Luhmann, J., Roelof, E., Williams, D., Livi, S., Curtis, C.C., Hsieh, K.C., Sandel, B.R., Grande, M., Carter, M., Sauvaud, J.-A., Fedorov, A., Thocaven, J.-J., Orsini, S., Cerulli-Irelli, R., Maggi, M., Wurz, P., Bochsler, P., Krupp, N., Woch, J., Fraenz, M., Asamura, K., Dierker, C., 2006. First ENA observations at Mars: Subsolar ENA jet. Icarus 182, 413–423.

Holmström, M., Barabash, S., Kallio, E., 2002. Energetic neutral atoms at Mars. 1. Imaging of solar wind protons. J. Geophys. Res. 107 (A10), doi:10.1029/2001JA000325. 1277.

Kallio, E., Barabash, S., 2000. On the elastic and inelastic collisions between precipitating energetic hydrogen atoms and martian atmospheric neutrals. J. Geophys. Res. 105 (A11), 24973–24996.

Kallio, E., Barabash, S., 2001. Atmospheric effects of precipitation energetic hydrogen atoms on the martian atmosphere. J. Geophys. Res. 106 (A1), 165–177.

Kallio, E., Janhunen, P., 2001. Atmospheric effects of proton precipitation in the martian atmosphere and its connection to the Mars–solar wind interaction. J. Geophys. Res. 106 (A4), 5617–5634.

Lichtenegger, H., Lammer, H., Stumptner, W., 2002. Energetic neutral atoms at Mars. 3. Flux and energy distributions of planetary energetic H atoms. J. Geophys. Res. 107 (A10), doi:10.1029/2001JA000322. 1279.

Luhmann, J.G., Bauer, S.J., 1992. Solar wind effects on atmosphere evolution at Venus and Mars. In: Luhmann, J.G., Tatrallyay, M., Pepin, R.O. (Eds.), Venus and Mars: Atmospheres, Ionospheres, and Solar Wind Interaction. In: AGU Geophysical Monographs, vol. 66, pp. 417–430.

Lundin, R., Barabash, S., Andersson, H., Holmström, M., Grigoriev, A., Yamauchi, M., Sauvaud, J.-A., Fedorov, A., Budnik, E., Thocaven, J.-J., Winningham, D., Frahm, R., Scherrer, J., Sharber, J., Asamura, K., Hayakawa, H., Coates, A., Linder, D.R., Curtis, C., Hsieh, K.C., Sandel, B.R., Grande, M., Carter, M., Reading, D.H., Koskinen, H., Kallio, E., Riihela, P., Schmidt, W., Säles, T., Kozyra, J., Krupp, N., Woch, J., Luhmann, J., McKenna-Lawler, S., Cerulli-Irelli, R., Orsini, S., Maggi, M., Mura, A., Milillo, A., Roelof, E., Williams, D., Livi, S., Brandt, P., Wurz, P., Bochsler, P., 2004. Solar wind-induced atmospheric erosion at Mars: First results from ASPERA-3 on Mars Express. Science 305, 1933–1936.

Mura, A., Milillo, A., Orsini, S., 2002. Energetic neutral atoms at Mars. 2. Imaging of the solar wind–Phobos interaction. J. Geophys. Res. 107 (A10), doi:10.1029/2001JA000328. 1278.

Vignes, D., Mazelle, C., Rème, H., Acuña, M.H., Connerney, J.E.P., Lin, R.P., Mitchell, D.L., Cloutier, P., Crider, D.H., Ness, N.F., 2000. The solar wind interaction with Mars: Locations and shapes of the bow shock and the magnetic pile-up boundary from the observations of the MAG/ER experiment onboard Mars Global Surveyor. Geophys. Res. Lett. 27 (1), 49–52.